Electronic Supplementary Information

Intercalation of Cobaltocene into WS$_2$ Nanosheets for Enhanced Catalytic Hydrogen Evolution Reaction

In Hye Kwak,[†,a] *Hafiz Ghulam Abbas,*[†,b] *Ik Seon Kwon,*[†,a] *Yun Chang Park,*[c] *Jaemin Seo,*[a] *Min Kyung Cho,*[d] *Jae-Pyoung Ahn,*[d] *Hee Won Seo,*[a] *Jeunghee Park,*[*,a] *and Hong Seok Kang*[*,e]

[a] Department of Advanced Materials Chemistry, Korea University, Sejong 339-700, Republic of Korea; E-mail: parkjh@korea.ac.kr

[b] Department of Nanoscience and Nanotechnology, Jeonbuk National University, Chonju, Chonbuk 560-756, Republic of Korea

[c] Measurement and Analysis Division, National Nanofab Center (NNFC), Daejeon 305-806, Republic of Korea

[d] Advanced Analysis Center, Korea Institute of Science and Technology, Seoul 136-791, Republic of Korea

[e] Department of Nano and Advanced Materials, College of Engineering, Jeonju University, Chonju, Chonbuk 560-759, Republic of Korea; E-mail: hsk@jj.ac.kr

† I.H.K., H.G.A., and I. S.K equally contribute.

Contents

IV. References

I. Experimental Section

Synthesis. All reactants were purchased from Sigma-Aldrich. 88 mg (0.254 mmol) of Ammonium tetrathiotungstate ($(NH_4)_2WS_4$, molecular weight (MW) = 260.28 g mol^{-1}, 99.97%) and 4.8-48 mg (0.0254-0.254 mmol) of cobaltocene (bis(cyclopentadienyl) cobalt (II), $Co(C_5H_5)_2$, MW = 189.12 g mol^{-1}) are added into 10 mL of oleylamine ($C_{18}H_{35}NH_2$, OA, MW = 267.49 g mol^{-1}) in a 50 mL three-neck flask. Non-intercalated WS_2 nanosheets were also synthesized under the same growth condition without $CoCp_2$. The thermal decomposition of $(NH_4)_2WS_4$ would produce WS_2, which is described as (i) $(NH_4)_2WS_4 \rightarrow WS_3 + 2NH_3 + H_2S$; (ii) $WS_3 \rightarrow WS_2 + S$.[S1] The $CoCp_2$ can catalyse the reduction step (ii) by injection of the electron into the WS_3. The reaction mixture is degassed at 100 °C for 30 min. Then, the solution is heated to 280 °C under Ar environment at a rate of 10 °C min^{-1}. When the temperature reaches to 280 °C, the color of reaction solution turns from yellowish green to dark black. The reaction temperature is maintained at 280 °C for an hour. Next, anhydrous ethanol is added into the reaction mixture while cooling down the reaction mixture to room temperature. The reaction solution is precipitated using centrifugation at 6000 rpm for 10 min. Purification process via precipitation is conducted by 5 times using ethanol (2) toluene (2), and acetone (1). The black powders were obtained after drying under vacuum.

Characterization. The products were characterized by scanning electron microscopy (SEM, Hitachi S-4700), and field-emission transmission electron microscopy (FE TEM, FEI TECNAI G2 200 kV, Jeol JEM 2100F, HVEM). Energy-dispersive X-ray fluorescence spectroscopy (EDX) with elemental maps was measured using a TEM (FEI Talos F200X) operated at 200 keV that equipped with high-brightness Schottky field emission electron source (X-FEG) and Super-X EDS detector system (Bruker Super-X). Fast Fourier-transform (FFT) images were

generated by the inversion of the TEM images using Digital Micrograph GMS1.4 software (Gatan Inc.).

High-resolution TEM (HRTEM)/STEM system equipped with a probe Cs corrector (JEM-ARM 200F with Schottky type FEG operated at 200 kV equipped with CEOS Cs-corrector) was used to obtain the high-angle annular dark-field (HAADF) and annular bright-field (ABF) STEM images. The electron energy loss spectroscopy (EELS) experiments were carried out using an Enfina system from Gatan Inc., respectively. Cs-corrected STEM analysis was also carried out using a Titan 80-300™ (FEI, The Netherlands) microscope operated at 300 kV. The STEM convergence semi-angle (α) used was ~18 mrad. The STEM minimum and maximum acceptance semi-angles (β) were ~20 and 122 mrad, respectively.

High-resolution X-ray diffraction (XRD) patterns were obtained using the 9B and 3D beamlines of the Pohang Light Source (PLS) with monochromatic radiation (λ = 1.54595 Å). XRD pattern measurements were also carried out in a Rigaku D/MAX-2500 V/PC using Cu K_α radiation (λ = 1.54056 Å). X-ray photoelectron spectroscopy (XPS) measurements were performed using the 8A1 beam line of the PLS, as well as a laboratory-based spectrometer (Thermo Scientific Theta Probe) using a photon energy of 1486.6 eV (Al Kα).

X-ray absorption near edge spectra (XANES) and extended X-ray absorption fine structure (EXAFS) spectra at the W L_3-edge and Co K-edge were collected in transmission mode using the 10C beam line of the PLS with a ring current of 350 mA at 3.0 GeV. Energy calibration was carried out by simultaneously measuring the reference spectrum of W and Co metal foils. Least-squares fits of EXAFS data were performed using the Athena and Artemis software packages, version 0.9.25.

Inductively coupled plasma atomic emission spectrometry (ICP-AES) was performed on a ThermoFisher iCAP-7600. Solid-state ^{13}C (100.64 MHz) NMR spectra were acquired on a Bruker AVANCE II$^+$ 400 MHz NMR system (at the KBSI Seoul Western Center) equipped with a Bruker 3.2 mm bore HXY probe operating in HX mode. The magic angle spinning ^{13}C NMR experiments (one pulse method) were performed using a pulse length of 2 μs for a π/2 pulse length of 5 μs, and a pulse repetition delay time of 3 s. The spectra were referenced to an external adamantane standard in which the peak at higher chemical shift was set at 38.43 ppm. The spectra were processed using the Bruker Topspin software (version 3.2) using conventional techniques, and a 50 Hz line broadening window function was applied in all cases.

Electron paramagnetic resonance (EPR) measurements were performed on a Bruker EMX-Plus spectrometer at room temperature. The samples (4 mg) were loaded in a quartz tube. The microwave frequency was 9.644564 GHz, and the microwave power was fixed to 20 mW to avoid saturation. Attenuated total reflectance Fourier transform infrared (ATR FTIR) spectra were obtained on a LabRam ARAMIS IR^2 (HORIBA JOBIN YVON). Spectra were collected by pressing the sample onto a diamond crystal with a pressure setting of 90 on the DuraScope. Each spectrum consisted of 16 spectra co-added accumulated between 4000 cm^{-1} and 560 cm^{-1} with a spectral resolution of 4 cm^{-1}. Raman spectra were measured with a micro-Raman spectrometer (Horiba ARAMIS IR2), using a diode laser with an excitation wavelength of 532 nm.

Electrochemical Measurements. Experiments were carried in a three-electrode cell connected to an electrochemical analyzer (CompactStat, Ivium Technologies). HER electrocatalysis (in 0.5 M H_2SO_4 electrolyte) was measured using a linear sweeping from 0 to -0.8 V (vs. RHE) with a scan rate of 2 mV s^{-1}. A saturated calomel electrode (SCE, KCl saturated, Basi Model

RE-2BP) was used as reference electrode, and a graphite rod (6 mm dia. × 102 mm long, 99.9995%, Pine Instrument) was used as counter electrode. The electrolyte was purged with H_2 (ultrahigh grade purity) during the measurement. The applied potentials (E) reported in our work were referenced to the reversible hydrogen electrode (RHE) through standard calibration. In 0.5 M H_2SO_4 electrolyte (pH 0), E (vs. RHE) = E (vs. SCE) + E_{SCE} (= 0.241 V) + 0.0592 pH = E (vs. SCE) + 0.241 V. The overpotential (η) was defined as E (vs. RHE). 4 mg sample was mixed with 1 mg carbon black (Vulcan XC-72) dispersed in Nafion (20 µL) and isopropyl alcohol (0.98 mL). The catalyst materials (0.390 mg cm^{-2}) were deposited on a glassy carbon (GC) rotating disk electrode (RDE, area = 0.1641 cm^2, Pine Instrument), and a rotation speed of 1600 rpm was used for the linear sweep voltammetry (LSV) measurements. The Pt/C (20 wt.% Pt in Vulcan carbon black, Aldrich-Sigma) tested as reference sample using the same procedure.

Electrochemical impedance spectroscopy (EIS) measurements were carried out for the electrode in an electrolyte by applying an AC voltage of 10 mV in the frequency range of 100 kHz to 0.1 Hz at a bias voltage of -0.15 V (vs. RHE). To measure double-layer capacitance, a potential range in which no apparent Faradaic processes occur was determined from static via cyclic voltammograms (CV). This range is 0.1–0.2 V. All measured current in this non-Faradaic potential region is assumed to be due to double-layer capacitance. The charging current, i_c, is then measured from CVs at multiple scan rates. The working electrode was held at each potential vertex for 10 s before beginning the next sweep. The current density (J) is equal to the product of the scan rate (ν) and the electrochemical double-layer capacitance (C_{dl}), as given by equation $J = ν\,C_{dl}$, Thus, a plot of J as a function of ν yields a straight line with a slope equal to C_{dl}. The scan rates were 20–100 mV s^{-1}.

TOF Calculation. The active site density and per-site turnover frequency (TOF) have been estimated as follows. It should be emphasized that since the nature of the active sites of the catalysts is not clearly understood yet and the real surface area for the nanostructured heterogeneous catalyst is hard to accurately determine, the following result is really just an estimation.

To estimate the electrochemically active surface site density, we used the C_{dl} value determined by CV measured at 0.1-0.2 V, in a non-Faradaic region, using various scan rates; 5.8, 22.5, and 10.2 mF cm^{-2}, respectively, for 7%, 14%, and 20% CoCp$_2$-intercalated WS$_2$. The roughness factor, which is basically the surface area ratio between the catalyst vs. the metal electrodes (0.035 mF cm^{-2}),[S2] is calculated as 165 (= 5.8 mF cm^{-2}/0.035 mF cm^{-2}), 643, and 291 for 7%, 14%, and 20% CoCp$_2$-intercalated WS$_2$, respectively.

The number of catalytic sites on the flat surface of catalyst can be estimated based on the crystal structure of distorted octahedral-phase 1T' WS$_2$. Using the lattice parameters of 1T' phase WS$_2$ (we calculated as a = 3.27 Å, b = 3.20 Å, γ = 119°) and assuming one active site per WS$_2$ (which translates into on reactive sites per unit cell), the density of surface active sites is 1/(0.5 × 3.27 × 3.20 × sin 119°) × 10^{16} cm^{-2} = 2.2 × 10^{15} atom cm^{-2}.[S3] Our DFT calculation shows that the basal S sites above the center site (Co) of CoCp$_2$ are the most active sites, so the number of surface active sites is calculated as 0.14 (or 0.07, 0.20) × 2.2 × 10^{15} cm^{-2}, for 14% (or 7%, 20%) CoCp$_2$-intercalated WS$_2$. The density of surface active sites (m) of WS$_2$-CoCp$_2$ (14%) on geometric area: 0.14 × 2.2 × 10^{15} atom cm^{-2} × roughness factor (= 643) = 2.0 × 10^{17} cm^{-2}.

The total number of hydrogen (H$_2$) gas turns overs was calculated from the current density (J in mA cm^{-2}) according to n_{H2} = J (mA cm^{-2})/1000 mA × 1 C s^{-1} × 1 mol e$^-$/96486 C × (1 mol

H_2/2 mol e^{-1}) $\times$ (6.022$\times10^{23}$ H_2 molecules/1 mol H_2) = 3.12 $\times$ 10^{15} H_2 s^{-1} cm^{-2} per mA cm^{-2}.

For WS$_2$-CoCp$_2$ (14%), the TOF for J = 30 mA cm^{-2} at η = 0.2 V is n_{H2}/m = 30 $\times$ 3.12 $\times$ 10^{15} H_2 s^{-1} cm^{-2} / 2.0 $\times$ 10^{17} cm^{-2} = 0.47 H_2 s^{-1}. We summarized the TOF values at 0.2 V as follows.

Concentration of CoCp$_2$	J (mA cm^{-2}) at η = 0.2 V	n_{H2} (s^{-1} cm^{-2})	Roughness factor	m (cm^{-2})	TOF (s^{-1})
7%	3.2	1.0 $\times$ 10^{16}	165	2.5 $\times$ 10^{16}	0.40
14%	30	9.4 $\times$ 10^{16}	643	2.0 $\times$ 10^{17}	0.47
20%	18	5.8 $\times$ 10^{16}	291	1.3 $\times$ 10^{17}	0.45

Computations. Geometry optimizations were performed using the Vienna ab-initio simulation package (VASP).[S4] The electron-ion interactions were described using the projector-augmented wave (PAW) method.[S5] Attractive van der Waals interactions were included using Grimme's correction for the Perdew–Burke-Ernzerhof (PBE)-D3 method.[S6] For structural optimization, the atoms were relaxed in the direction of the Hellmann-Feynman force using the conjugate gradient method with an energy cut-off of 520 eV, until a stringent convergence criterion of 1 meV/Å was satisfied. Lattice constants were optimized using the PBE-D3 exchange-correlation functional.[S7] The k-point sampling was performed using Γ-centered 6×6×4 points, which gave the total energy of the (4×4) WS$_2$ complex in the 1T' phase within 1 meV.

The adsorption energies and activation barriers for an H^+ ion at different adsorption sites were calculated using the climbing image-nudged elastic band (CINEB) method.[S8] For simplicity, we employed a slab geometry in which a supercell included two WS$_2$ layers and one CoCp$_2$ molecule. The coordinate system is defined so that the WS$_2$ layer lies on the *ab* plane parallel to the XY plane. Two lowest sublayers (i.e., all W ions as well as one-half of S

atoms on the lower WS_2 layer) were fixed, while all other atoms were permitted to relax freely. For computational efficiency, we adopted a supercell of (4×4) $2WS_2$ with one $CoCp_2$ molecule. For the Volmer reaction, the c constant of the supercell perpendicular to the slab geometry was maintained at a sufficiently large value (31.08 Å). In the initial configuration (IC), a H^+ ion was placed far from the WS_2 surface so that its closest distances to two WS_2 image surfaces along the c direction were at least 6.10 and 7.05 Å, respectively. In Heyrovsky reaction, the same c constant was used to identify the activated complex (AC). In the next step, the supercell was further elongated along the c direction by 19.00 Å and the second H^+ ion was placed and separated from the two image surfaces by 9.00 and 10.00 Å in the IC of the reaction, so that the activation barrier can be estimated more accurately by improving the accuracy of the calculated energies of the IC and AC.

II. Supporting Tables

Table S1. Characteristics of WS$_2$ samples and their HER performance.

I^a	[CoCp$_2$]/[(NH$_4$)$_2$WS$_4$]	[CoCp$_2$]^b	[Co^{3+}]^c	[Co^{2+}]^d	$\eta_{J=10}{}^e$	b^f
None	0	0	0	0	0.36	120
CoCp$_2$	0.5	7	4.4	2.6	0.24	72
CoCp$_2$	1	14	8.2	5.8	0.17	40
CoCp$_2$	2	20	9.2	10.8	0.19	47

^{a} Intercalated molecules; ^{b} Concentration (%) of intercalated CoCp$_2$ ([CoCp$_2$]/[WS$_2$]) determined using EDX, XPS (Co 2p and W 4f peaks), and ICP-AES; ^{c} Concentration (%) of intercalated cation form ([Co^{3+}]/[WS$_2$]); ^{d} Concentration (%) of Co^{2+} form = [CoCp$_2$] − [Co^{3+}]; ^{e} HER overpotential (V) at J = 10 mA cm^{-2}; ^{f} Tafel slope (mV dec^{-1}) for HER.

Table S2. Fitting parameters of EXAFS data for the WS$_2$ samples (see **Figure 2** and **Figure S5**). The FT curves of EXAFS were fitted to two scattering shells. A least-squares curve parameter method was performed using the ARTEMIS module of IFEFFIT and USTCXAFS software packages.

	Sample	Scattering Path	R (Å)^a	CN^b	ΔE (eV)^c	σ^2 (Å^2)^d
W L$_3$-edge	2H WS$_2$	W-S	2.40540	6.0	6.479	0.00193
		W-W	3.18070	6.0	4.811	0.00320
	WS$_2$	W-S	2.39880	4.1 ± 0.7	5.398	0.00407
		W-W	2.76410	2.3 ± 1.2	4.036	0.00539
	WS$_2$-CoCp$_2$-7%	W-S	2.39810	3.3 ± 1.5	5.842	0.00671
		W-W	2.76152	3.1 ± 1.9	3.716	0.00581
	WS$_2$-CoCp$_2$-14%	W-S	2.39880	3.2 ± 1.0	5.328	0.00149
		W-W	2.76410	2.1 ± 2.1	-6.499	0.00490
	WS$_2$-CoCp$_2$-20%	W-S	2.40943	3.0 ± 2.0	4.830	0.00886
		W-W	2.75942	2.2 ± 2.0	3.518	0.00681
	CoCp$_2$	Co-C	2.04	10.4 ± 2.4	6.422	0.00508
Co K-	WS$_2$-CoCp$_2$-7%	Co-C	2.08	10.2 ± 2.1	5.962	0.00517

WS$_2$-CoCp$_2$-14%	Co-C	2.10	10.3 ± 2.2	4.817	0.00221
WS$_2$-CoCp$_2$-20%	Co-C	2.14	10.5 ± 2.3	4.114	0.01234

[a] Distance between scattering atoms. The FT curve of the 2H phase WS$_2$ are characterized by two main peaks at 2.40 and 3.18 Å, corresponding to the nearest W–S and W-W bonds, respectively. In contrast, in the FT curves of WS$_2$ and WS$_2$-CoCp$_2$, the distance of W–W bond is decreased to 2.76 Å.

[b] Coordination number of W atoms. Since the coordination number of W-W decreased from 6 (2H phase) to 2 (1T′ phase), the intensity of 1T′ phase WS$_2$ and WS$_2$-CoCp$_2$ is nearly reduced by 1/3. This result indicates that the WS$_2$ adopts a distorted octahedral coordination.

[c] Edge energy shift, representing between the energy grids of experimental and theoretical data.
[d] Debye-Waller factor, which measures the static and thermal disorder, is larger for the intercalated samples than 2H-WS$_2$. It suggests that the intercalation produces a broad range of W-S and W-W distances.

Table S3. Impedance parameters for the equivalent circuit that was shown in **Figure S8**, and the double-layer capacitance (C$_{dl}$) as shown in **Figure S9**.

`	EIS		C$_{dl}$ (mF cm^{-2})
Samples	R$_s$ (Ω)	R$_{ct}$ (Ω)	
WS$_2$	5.0	360	2.2
WS$_2$-CoCp$_2$-7%	5.2	69.1	5.8
WS$_2$-CoCp$_2$-14%	4.0	34.2	22.5
WS$_2$-CoCp$_2$-20%	4.5	42.3	10.2

**Table S4.** Comparison of HER performance (in pH 0) of WS_2 in the literatures (N/A: Not applicable).

| Reference	Materials	Phase	$E_{J=10}$ (mV) at 10 mA cm^{-2}	Tafel slope (mV dec^{-1})	TOF
S9	Exfoliated WS_2	1T	N/A (~280)	60	175 s^{-1} at 288 mV
S10	WS_2 nanoribbon	2H	225	68	N/A
S11	WS_2 Nanoflake	2H	N/A (~420)	48	N/A
S12	WS_2@heteroatom doped graphene	1T	125	52.7	N/A
S13	WS_2/Graphene	2H	229	73	N/A
S14	N doped WS_2	2H	N/A (~140)	69	0.725 s^{-1} at 108 mV
S15	CoS_2@WS_2/CC	2H	97.2	66	N/A
S16	WS_2@graphene	1T	260	45.4	N/A
S17	Colloidal WS_2	1T′	200	50	N/A
S18	Co:WS_2@Co:$W_{18}O_{49}$	1T	240	49	N/A
Present work	WS_2-$CoCp_2$	1T'	170	40	0.47 s^{-1} at 200 mV

III. Supporting Figures
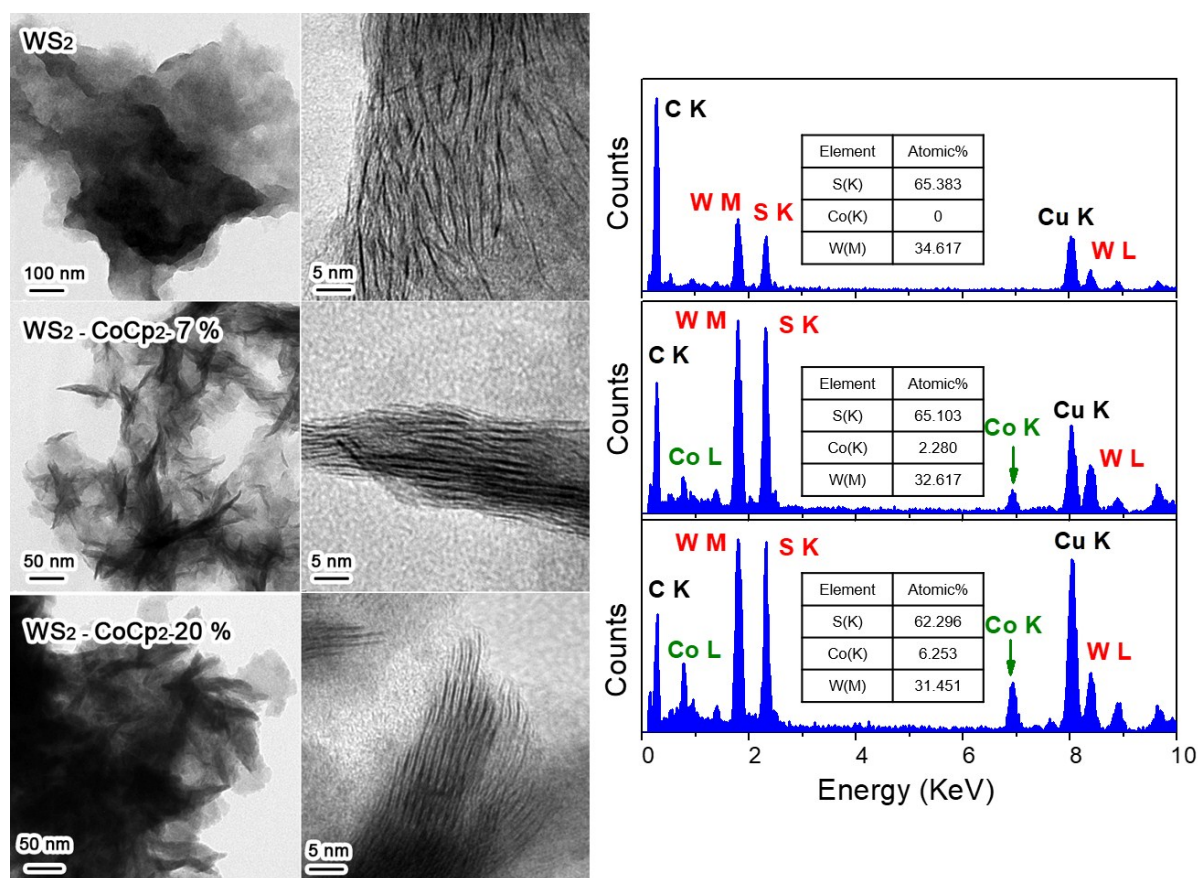
Figure S1. HRTEM images of WS_2, WS_2-$CoCp_2$-7%, and WS_2-$CoCp_2$-20% and their EDX spectrum showing that the atomic ratio of [Co]/[W] is 0%, 7%, and 20%, respectively.

The WS_2 nanosheets consisted of the aggregated thin layers. The distance between adjacent WS_2 layers (d_{002}) is in the wide range of 0.7-3 nm. The WS_2-$CoCp_2$ complexes exhibit the similar morphology in which the average size of nanosheets is 80 nm, and the average thickness is 10 nm. The atomically resolved TEM images show that the interlayer distance (d_{002}) is uniformly expanded to 11 Å. The EDX spectrum revealed the homogeneous distribution of the composition in the entire sample. The peaks of Co (K shell) and W (M shell) provides the ratio of $CoCp_2$ and WS_2.
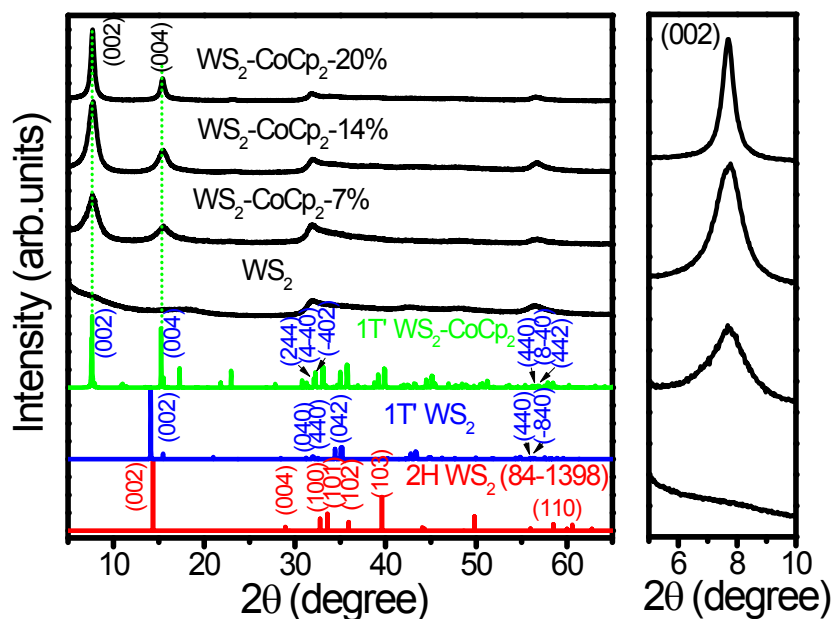
Figure S2. XRD pattern of WS_2 and WS_2-$CoCp_2$ complexes with 7%, 14%, and 20%. The peaks were referenced to those of 2H phase WS_2 (JCPDS Card 84-1398; a = 3.153 Å and c = 12.323 Å), 1T′ phase WS_2 (a = 3.26 Å, b = 3.19 Å, and c = 12.02 Å), and 1T′ phase WS_2-$CoCp_2$ (a = 3.26 Å, b = 3.19 Å, and c = 23.2 Å), as shown at the bottom.

VESTA program (http://jp-minerals.org/vesta/en/) was used to generate the simulated XRD pattern for 1T′ phase whose lattice parameters were obtained by the present calculation. The (002) and (004) peak position of WS_2-$CoCp_2$ complexes is matched well with that of the simulated XRD pattern of WS_2-$CoCp_2$. The broad peaks at 2θ = 32º and 57º are ascribed to the overlapped many peaks. For non-intercalated WS_2, the (002) and (004) peaks exhibit almost zero intensity, probably due to the wide range of interlayer distance as identified by the TEM data.
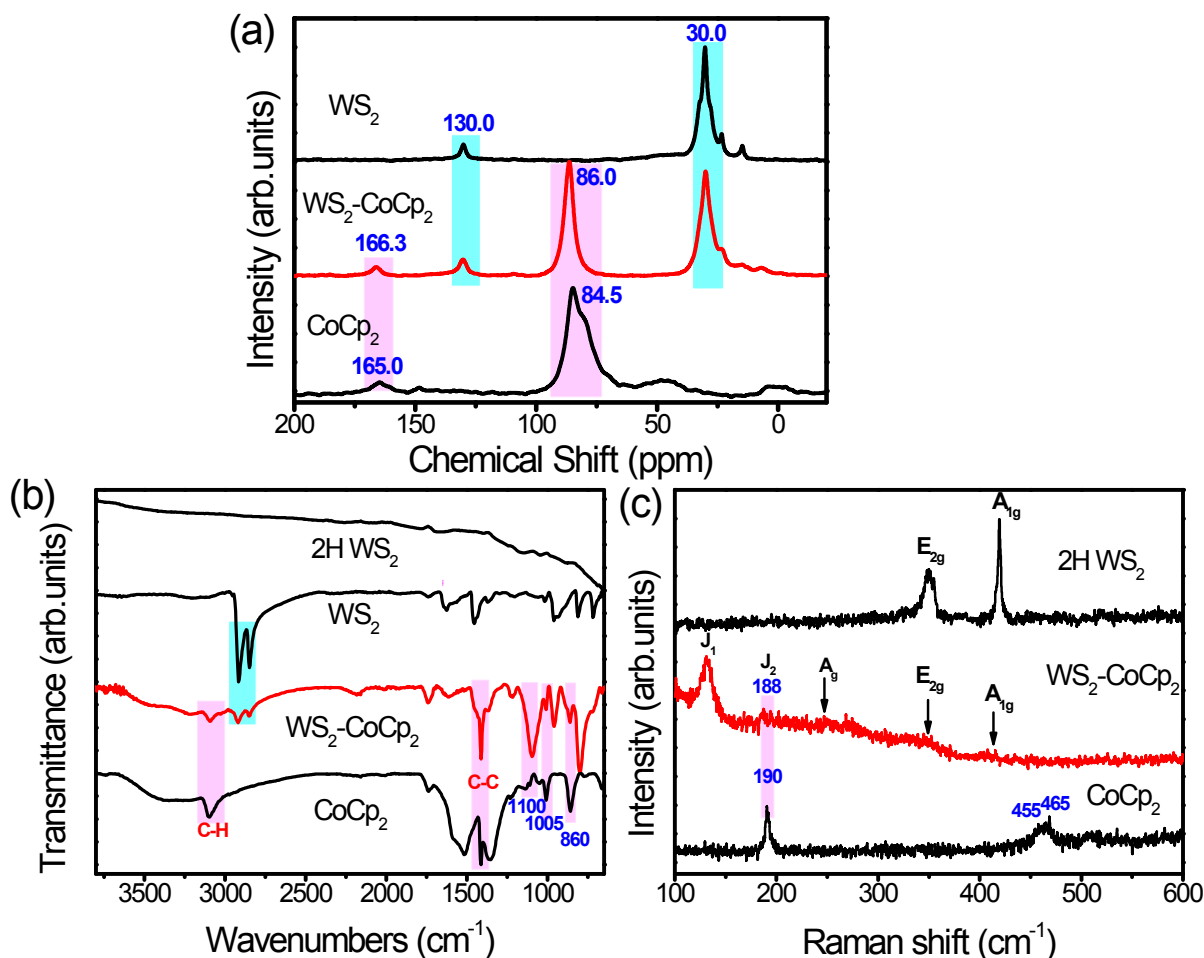
Figure S3. (a) Solid state ^{13}C NMR spectra of $CoCp_2$, WS_2, and WS_2-$CoCp_2$-14%. (b) IR spectrum of $CoCp_2$, WS_2-$CoCp_2$-14%, WS_2, and 2H phase WS_2 (2H-WS_2) powders. (c) Raman spectra of $CoCp_2$, WS_2-$CoCp_2$ -14%, and 2H-WS_2. The $CoCp_2$ and 2H-WS_2 powders were purchased from Sigma-Aldrich.

(a) The ^{13}C NMR spectrum of $CoCp_2$ powders (purchased from Sigma-Aldrich) show the C-C(=C) peak of cyclopentadienyl ring (Cp_2) of $CoCp_2$ at 84.5 and that of cationic form at 165 ppm. The WS_2-$CoCp_2$ shows those peaks at 86.0 and 166.3 ppm. The blue shift from the peaks of $CoCp_2$ could be due to the charge transfer from the Cp to WS_2. The peaks at 30.8 and 130.0 ppm can be assigned to the C-C and C=C of oleylamine, respectively, since the WS_2 shows the same peak.

(b) We assigned the IR peaks of $CoCp_2$ based on the references;[S19,S20] C-H stretching at 3090 cm^{-1}, C-C stretching at 1415 cm^{-1}, C-C breathing at 1100 cm^{-1}, C-C-H (in-plane) bending at

1005cm^{-1}, and C-H (out-of-plane) bending at 860 cm^{-1}. The peak at 1500 cm^{-1} is originated from the scissoring mode of water. The WS$_2$-CoCp$_2$ shows the same peaks; C-H at 3088 cm^{-1}, C-C at 1415 cm^{-1}, C-C at 1095 cm^{-1}, C-C-H at 1008 cm^{-1}, and C-H bending at 860 cm^{-1}. It is known that the last peak is sensitive to oxidation; the peak position of CoCp$_2$ and WS$_2$-CoCp$_2$ are close to those of cation form.[S19] The WS$_2$ shows the strong C-H peaks at 2915 and 2850 cm^{-1} are originated from the oleylamine. The WS$_2$-CoCp$_2$ also shows the same peaks.

Summary of IR peak assignment

Samples	C-H stretching	C-C stretching	C-C breathing	C-C-H (in-plane) bending	C-H (out-of-plane) bending
CoCp$_2$	3090	1415	1100	1005	860
WS$_2$-CoCp$_2$	3088	1415	1095	1008	860

(c) The 2H phase WS$_2$ exhibit two characteristic Raman peaks at 350 and 418 cm^{-1}, corresponding to the in-plane E$^1_{2g}$ and out-of-plane A$_{1g}$ vibration modes, respectively. The WS$_2$-CoCp$_2$ shows the peaks of 1T' phase: J$_1$ peak at 133 cm^{-1}, J$_2$ peak at 188 cm^{-1}, and A$_g$ at 258 cm^{-1}, with the E$^1_{2g}$ mode at 350 cm^{-1} and the A$_{1g}$ mode at 410 cm^{-1}.[S17] The CoCp$_2$ shows the Raman peaks at 190, 455, and 465 cm^{-1}, which can be assigned to the Cp ring deformation vibrational mode of CoCp$_2^+$, the Co-Cp bond stretching vibrational mode of CoCp$_2^+$, and ring tilt vibrational mode of CoCp$_2$, respectively.[S21] The peak of WS$_2$-CoCp$_2$ at 188 cm^{-1} could be also originated from the Cp ring deformation vibrational mode.
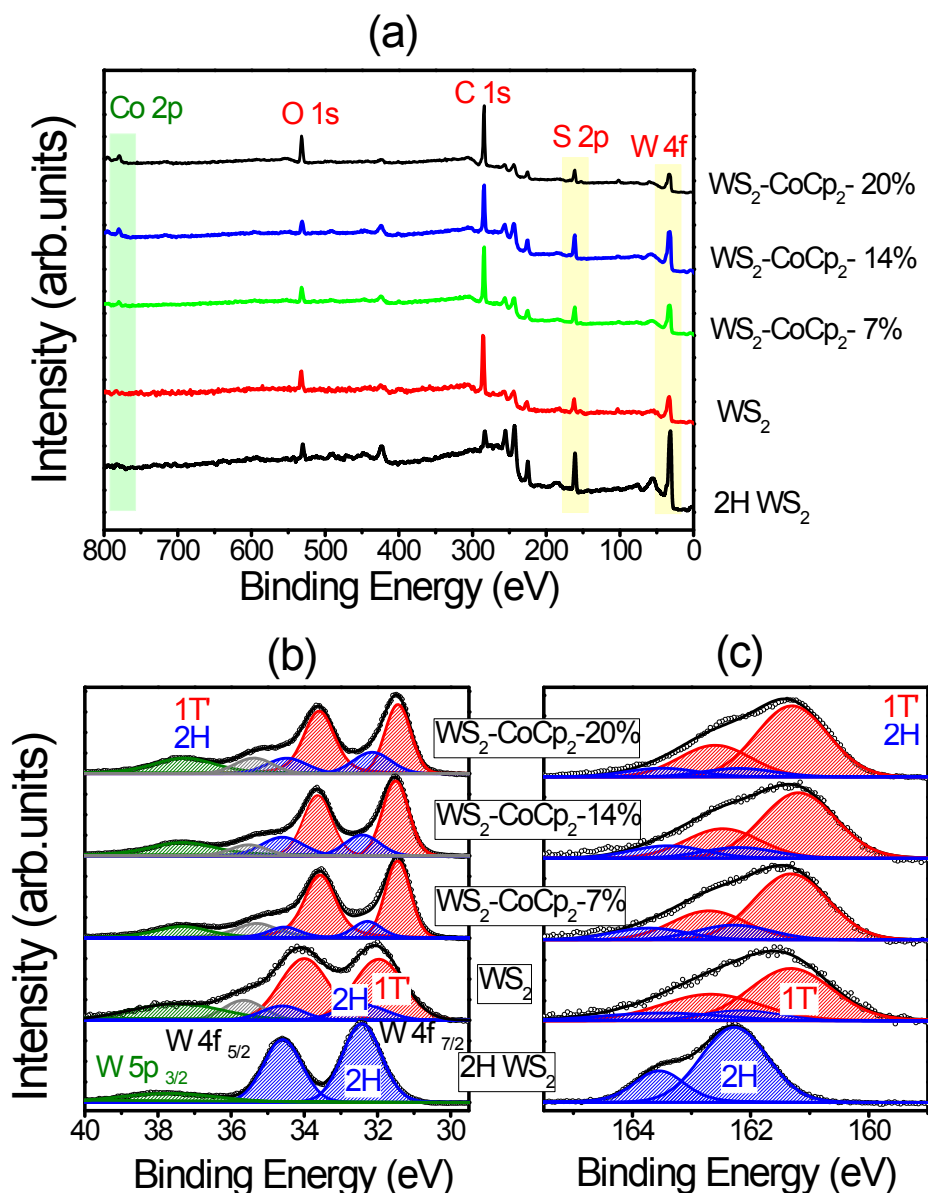
Figure S4. (a) Full-range XPS data of 2H-WS$_2$ (purchased from Sigma-Aldrich, 99.99%), WS$_2$, and WS$_2$-CoCp$_2$ (7%, 14%, and 20%). Fine-scanned (b) W 4f and W 5$p_{3/2}$ peaks and (c) S 2p peaks.

(a) The atomic ratio of [S]/[W] is 2 for all samples. For three WS$_2$-CoCp$_2$ samples, [Co]/[W] is 7, 14, and 20%. The C peak of WS$_2$ and WS$_2$-CoCp$_2$ is larger than that of 2H WS$_2$, due to the residual solvent and/or intercalated CoCp$_2$.

(b) The W 4$f_{7/2}$ and 4$f_{5/2}$ peaks (separated by about 2.18 eV), and W 5$p_{3/2}$ peak (green). The 2H-WS$_2$ shows the 4$f_{7/2}$ peak at 32.4 eV, which is 1 eV blue-shifted from the neural W at 31.4 eV. The 4$f_{7/2}$ peak of WS$_2$-CoCp$_2$ appears at 31.5 eV; this negligible shift is due to the metallicity

of 1T′ phase. The $4f_{7/2}$ peak was resolved into two bands: 1T' phase (red) at 31.5 eV and 2H phase (blue) at 32.4 eV. The fraction of the 1T′ phase was determined as avg. 80%, indicating that this is the major phase. The small peak (grey) at 35.6 eV is assigned to the defective bonding with oxygen.

(c) The S $2p_{3/2}$ and S $2p_{1/2}$ peaks, which are separated by about 1.2 eV. The 2H-WS$_2$ shows peaks at 162.3 and 163.5 eV, which are 1.7 eV red-shifted with respect to the signal of neutral S (S^0) at 164.0 and 165.2 eV. They correspond to the S^{2-} anions bonded with the W cations in the 2H phase. For the WS$_2$ and WS$_2$-CoCp$_2$ samples, the broad peak was resolved into four bands; two each for the 2H phase (blue) and the 1T' phase (red). The larger red-shift band, S $2p_{3/2}$ at 161.3 eV and S $2p_{1/2}$ at 162.5 eV, are assigned to those of electron-rich 1T' phase.
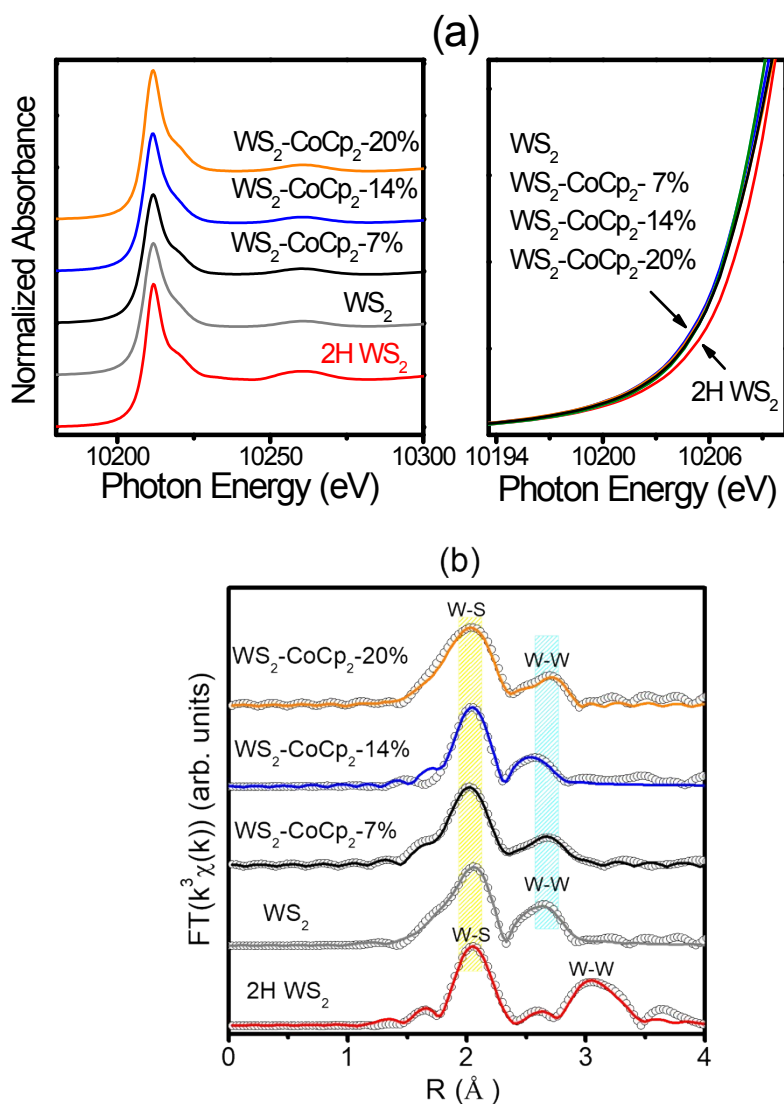
Figure S5. XANES spectra at the (a) W L_3 edge for 2H-WS$_2$ (purchased from Sigma-Aldrich, 99.99%), WS$_2$, and WS$_2$-CoCp$_2$ (7%, 14%, and 20%) and (b) non-phase-corrected k^3 weighted FT EXAFS data (open circles) of WS$_2$ and WS$_2$-CoCp$_2$ (7%, 14%, and 20%) at the W L_3 edge and their fitting curves (line).

(a) The evolution of the local crystal structure of samples was probed with W L_3 edge X-ray absorption near edge spectra (XANES) analysis. Magnified scaled spectrum reveals that edge energies of all samples are lower than those of 2H-WS$_2$. It suggests that the intercalation of CoCp$_2$ induces more metallic states of W.

(c) In the FT profiles (in real space), the EXAFS peaks indicate the distances to nearest neighbor atoms. The profiles of WS_2 and WS_2-$CoCp_2$ are significantly different from that of 2H-WS_2, suggesting a remarkable change in the local atomic arrangements due to the phase change to 1T′. The FT curves were fitted to two scattering shells, W–S and W–W bonds (see the parameters in **Table S2**). The shortest distance between W-S ($d_{W\text{-}S}$) and W-W ($d_{W\text{-}W}$) is 2.40 Å and 3.19 Å for the 2H-WS_2. All of WS_2 and WS_2-$CoCp_2$ shows $d_{W\text{-}S}$ = 2.40 Å and $d_{W\text{-}W}$ = 2.76 Å, consistently with the values of 1T′ phase.
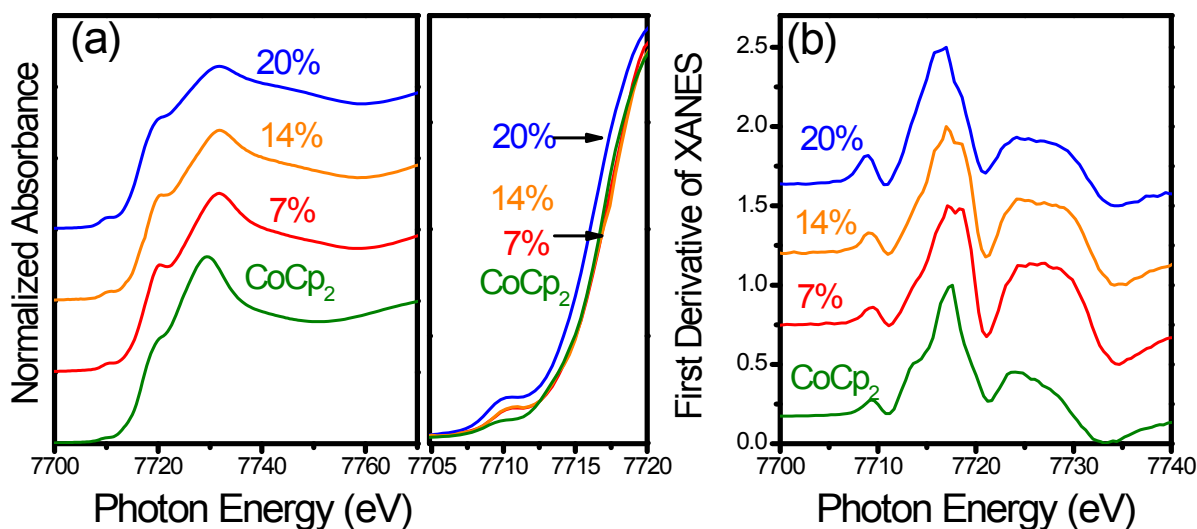
Figure S6. (a) XANES spectra of $CoCp_2$ powders and WS_2-$CoCp_2$ (7, 14, and 20%) at the Co K edge. (b) First derivative of absorbance curve in the onset region.

(a) The evolution of the local crystal structure of Co-containing samples was probed with the Co K edge XANES. The absorption edge in magnified scale shows a red shift for WS_2-$CoCp_2$-20%.

(b) The edge position was deduced from the first derivative of absorption curve in the onset region. The position of $CoCp_2$ powders is 7717.40 eV, which is blue shifted from than that of complexes, probably due to the higher concentration of cation ($CoCp_2^+$). The $CoCp_2$ powder underwent the oxidation and exist as the cationic complexes with hydroxide. It should be noted that the data of $CoCp_2$ powder is just used as the reference to assign the peak. As the concentration of $CoCp_2$ increases, the position shift to the lower energy; 7717.28, 7717.25, and 7716.79 eV for 7%, 14%, and 20%, respectively, indicating that the oxidation number decreases due to the increased concentration of neutral form, which is consistent with the EXAFS and XPS data.
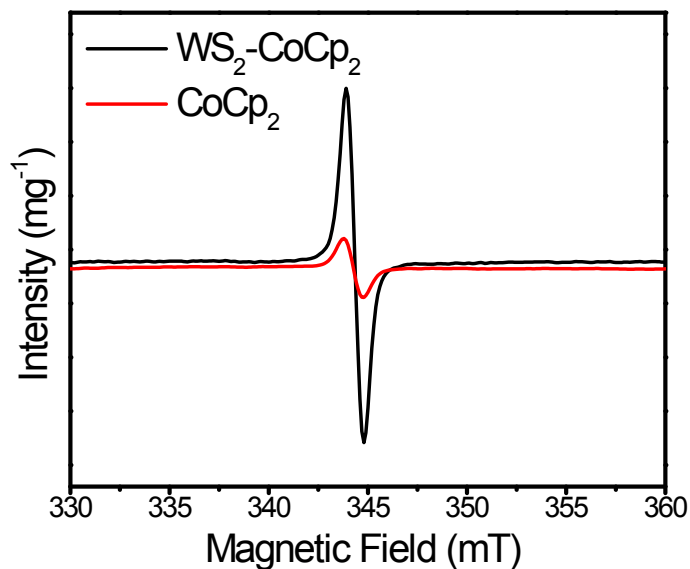
Figure S7. Electron paramagnetic resonance (EPR) spectra for $CoCp_2$ and WS_2-$CoCp_2$ (14%).

EPR measurements were performed for $CoCp_2$ and WS_2-$CoCp_2$ at room temperature. Both $CoCp_2$ precursor and WS_2-$CoCp_2$ exhibit a single peak, centered at 344 mT (g = 2.00). The signal can be originated from the low spin of Co^{2+} state in $CoCp_2$ neutral molecule.[S22] The larger intensity of WS_2-$CoCp_2$ than that of $CoCp_2$ is ascribed to the higher population of neutral form, consistently with the XPS, EXAFS, IR, and Raman data.
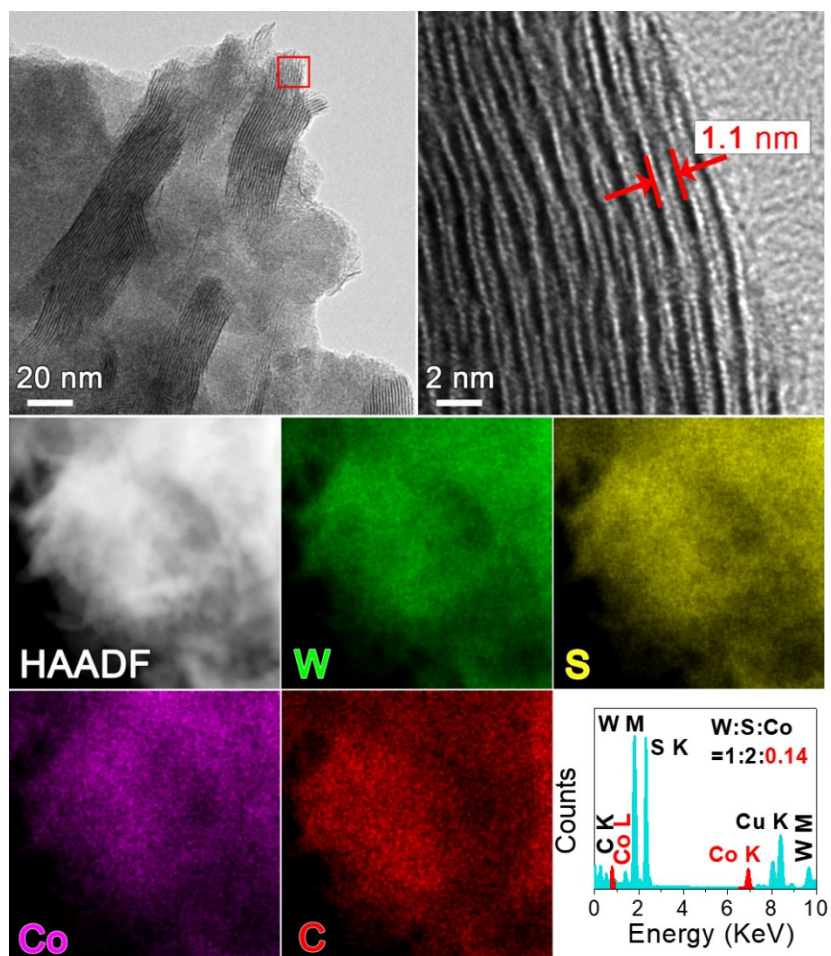
Figure S8. TEM images and EDX data of WS$_2$-CoCp$_2$-14% samples after 12h chronoamperometric measurement.

The average size (80 nm) and thickness (20 nm) of nanosheets are similar with those of the samples before HER. The lattice-resolved TEM image shows that the average distance between adjacent WS$_2$ layers (d_{002}) is the same as that of the before samples; 1.1 nm. The EDX mapping and spectrum show that the Co atoms distribute homogeneously over the entire samples with 14%, which remain the same after the HER.
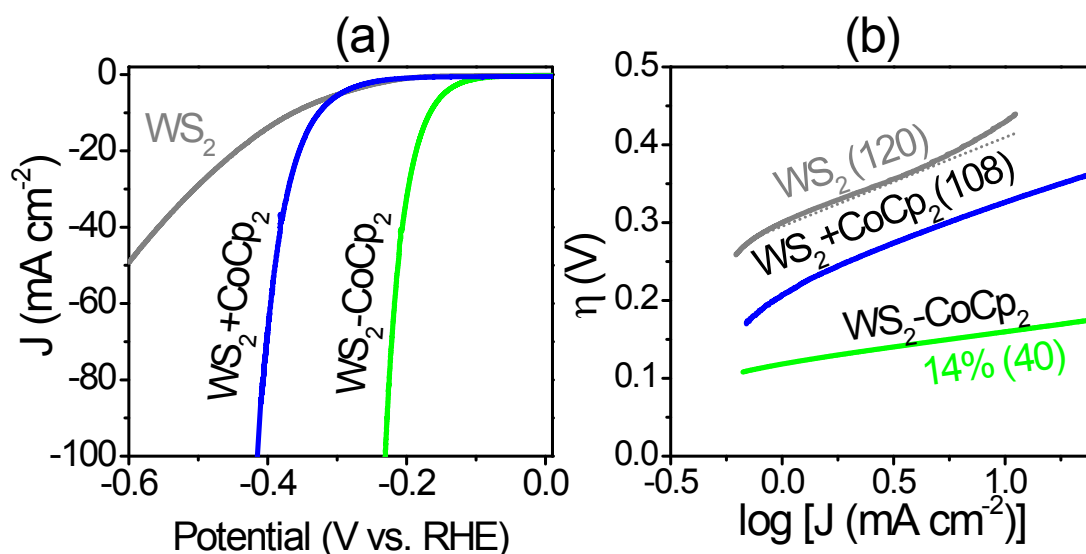
Figure S9. (a) LSV curves (scan rate: 2 mV s^{-1}) for a physical mixture of WS_2 and 14% $CoCp_2$ molecules (referred to as WS_2+$CoCp_2$) in H_2-saturated 0.5 M H_2SO_4. The data of WS_2 and WS_2-$CoCp_2$-14% is plotted for comparison. The overpotential for a current density of 10 mA cm^{-2} is 0.32 V, which is close to 0.36 V of WS_2. (b) Tafel plot derived from the LSV curve, where the Tafel slope is indicated in parentheses. The Tafel slope is 108 mV dec^{-1}, which is close to 120 mV dec^{-1} of WS_2.
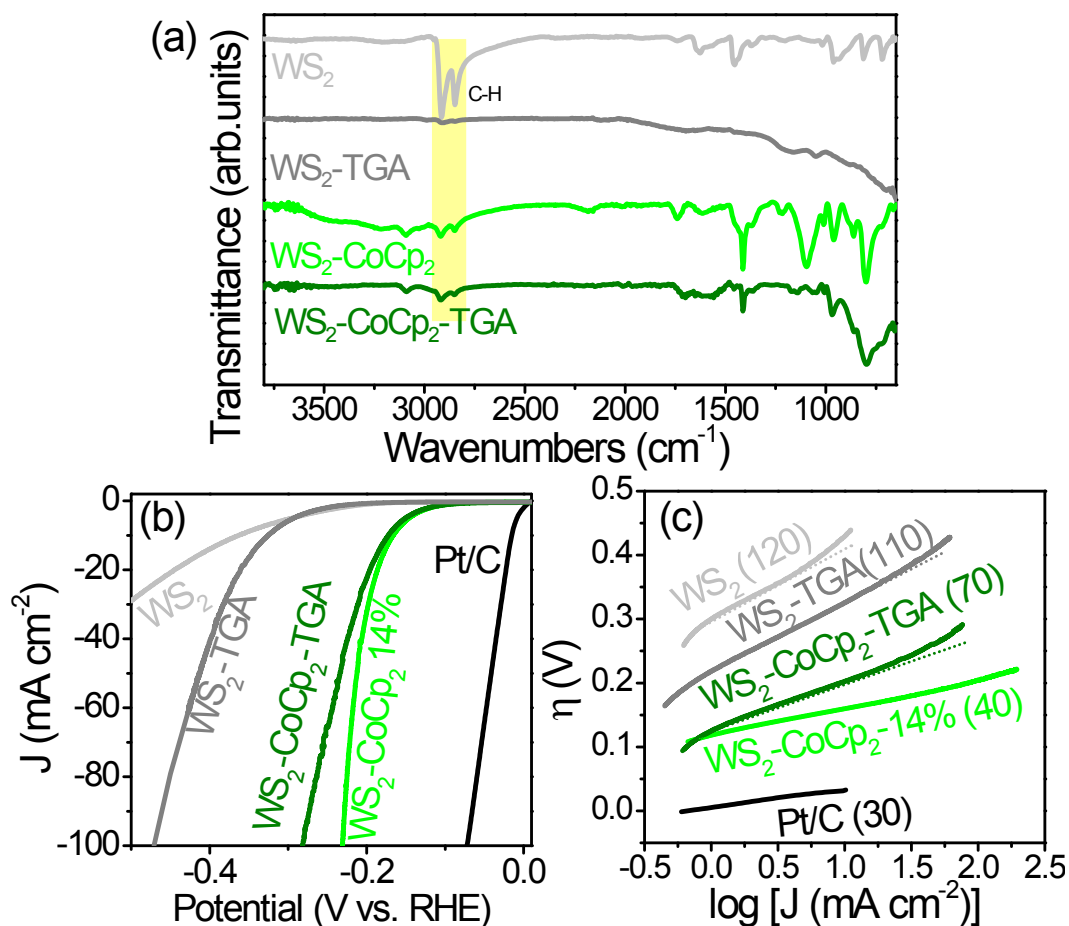
Figure S10. (a) FTIR spectrum of WS_2 and WS_2-$CoCp_2$-14% before and after treatment with thioglycolic acid (TGA). The after samples were referred to as WS_2-TGA and WS_2-$CoCp_2$-14%-TGA. (b) LSV curves (scan rate: 2 mV s^{-1}) for WS_2-TGA and WS_2-$CoCp_2$-14%-TGA in H_2-saturated 0.5 M H_2SO_4. The data of the before samples is plotted for comparison. (c) Tafel plot derived from the LSV curve, where the Tafel slope is indicated in parentheses.

(a) The as-synthesized powders (30 mg) were dispersed in anhydrous ethanol 50 mL and TGA (Sigma-Aldrich, 99%) 3 mL was added in the solution.[S23] The mixture was vigorously stirred at room temperature for 12h under argon gas flow, and then washed with ethanol by several times. The intensity of oleylamine peak is significantly reduced after the TGA treatments.

(b), (c) The overpotential for a current density of 10 mA cm^{-2} is 0.36 and 0.32 V, respectively, for WS_2 and WS_2-TGA. The Tafel slope is 70 and 110 mV dec^{-1} for WS_2 and WS_2-TGA. So the HER performance can be improved by the elimination of oleylamine ligand. In the case of WS_2-$CoCp_2$-14%, the HER performance was slightly reduced after the TGA treatment: the

overpotential for a current density of 10 mA cm^{-2} is 0.17 V, and the Tafel slope is 40 and 70 mV dec^{-1}, respectively, for before and after the TGA treatment. Nevertheless, the HER catalytic activity of WS$_2$-CoCp$_2$-14% is still higher than that of non-intercalated WS$_2$ after the ligand elimination. This result confirmed the enhancement effect of the CoCp$_2$ intercalation in the HER performance.
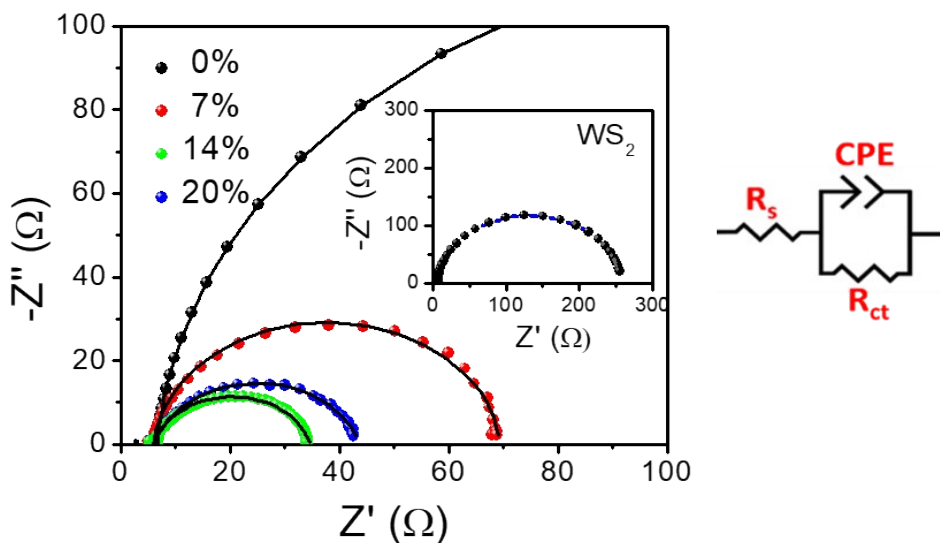
Figure S11. Nyquist plots for EIS measurements of WS$_2$ (including the inset) and WS$_2$-CoCp$_2$ (7%, 14%, and 20%) from 100 kHz to 0.1 Hz at a representative potential of -0.15 V (vs. RHE). The modified Randles circuit for fitting is shown on the right.

Electrochemical impedance spectroscopy (EIS) measurements of the samples were performed using a 100 kHz–0.1 Hz frequency range and an amplitude of 10 mV at $\eta = 0.15$ V. In the high-frequency limit and under non-Faradaic conditions, the electrochemical system is approximated by the modified Randles circuit shown on the right panel, where R_s denotes the solution resistance, CPE is a constant-phase element related to the double-layer capacitance, and R_{ct} is the charge-transfer resistance from any residual Faradaic processes. A semicircle in the low-frequency region of the Nyquist plots represents the charge transfer process, with the diameter of the semicircle reflecting the charge-transfer resistance. The real (Z') and negative imaginary ($-Z''$) components of the impedance are plotted on the x and y axes, respectively. The simulation of the EIS spectra using an equivalent circuit model allowed us to determine the charge transfer resistance, R_{ct}, which is a key parameter for characterizing the catalyst-electrolyte charge transfer process. The fitting parameters are listed in **Table S3**. The obtained R_{ct} values of WS$_2$, WS$_2$-CoCp$_2$-7%, WS$_2$-CoCp$_2$-14%, and WS$_2$-CoCp$_2$-20% are 360, 69.1, 34.2, and 42.3 Ω, respectively, showing a significant decrease upon intercalation of CoCp$_2$. The R_{ct} is consistent with that of the HER performance. The reduced charge-transfer resistance plays a major role in enhancing the HER catalytic activity of the intercalated samples.
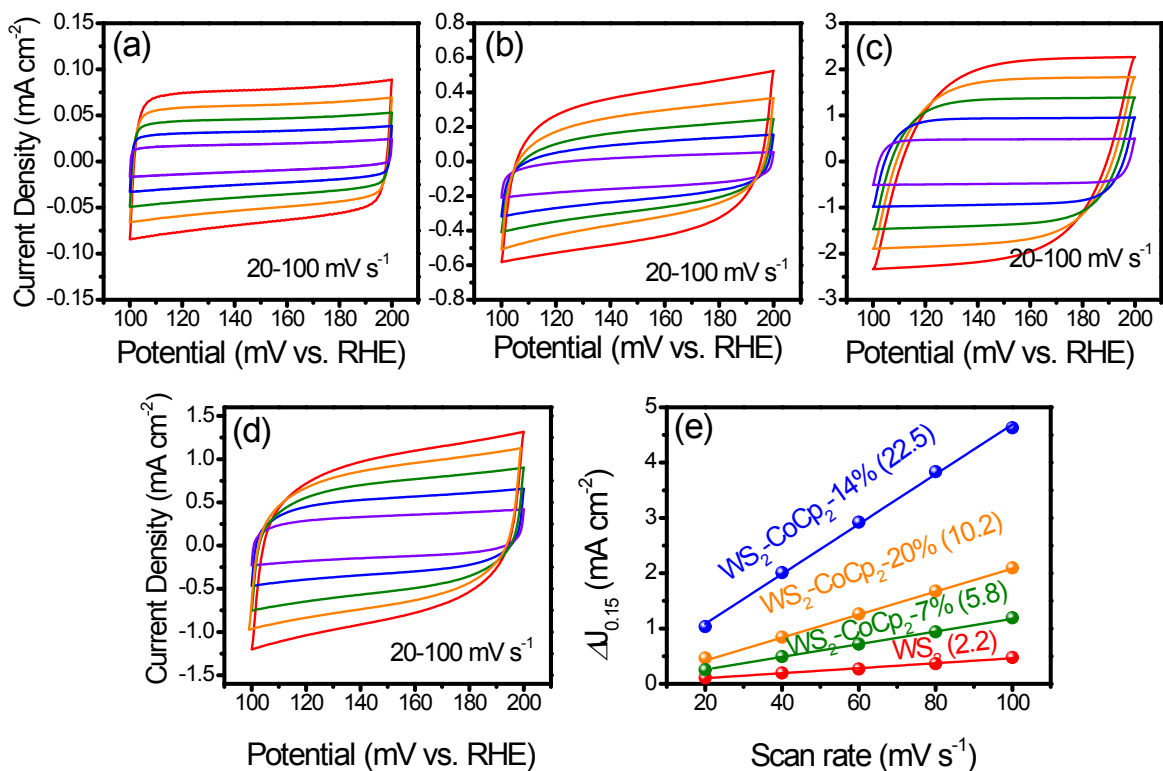
Figure S12. Cyclic voltammograms of (a) WS_2, (b) WS_2-$CoCp_2$-7%, (c) WS_2-$CoCp_2$-14%, and (d) WS_2-$CoCp_2$-20% in a non-Faradaic region (0.1-0.2 V vs. RHE), at 20-100 mV s^{-1} scan rates (with a step of 2 mV) and in 0.5 M H_2SO_4 solution. (e) Difference (ΔJ) between the anodic charging and cathodic discharging currents measured at 0.15 V (vs. RHE) and plotted as a function of the scan rate. The value in parenthesis represents the C_{dl}, obtained by the half of the linear slope.

Cyclic voltammograms (CV) were measured at 0.1-0.2 V, in a non-Faradaic region, using various scan rates. The double-layer capacitance (C_{dl}) was obtained as the slope of a linear fit of ΔJ vs. scan rate (20−100 mV s^{-1}), where ΔJ is the difference between the anodic charging and cathodic discharging currents. The C_{dl} values of WS_2, WS_2-$CoCp_2$-7%, WS_2-$CoCp_2$-14%, and WS_2-$CoCp_2$-20% are 2.2, 5.8, 22.5, and 10.2 mF cm^{-2}, respectively (see the summary in **Table S3**), showing a significant increase upon intercalation. The intercalated samples have very rough surfaces and can thus expose a large number of active sites. Therefore, the increased double-layer capacitance leads to the enhanced HER catalytic activity of the intercalated samples.
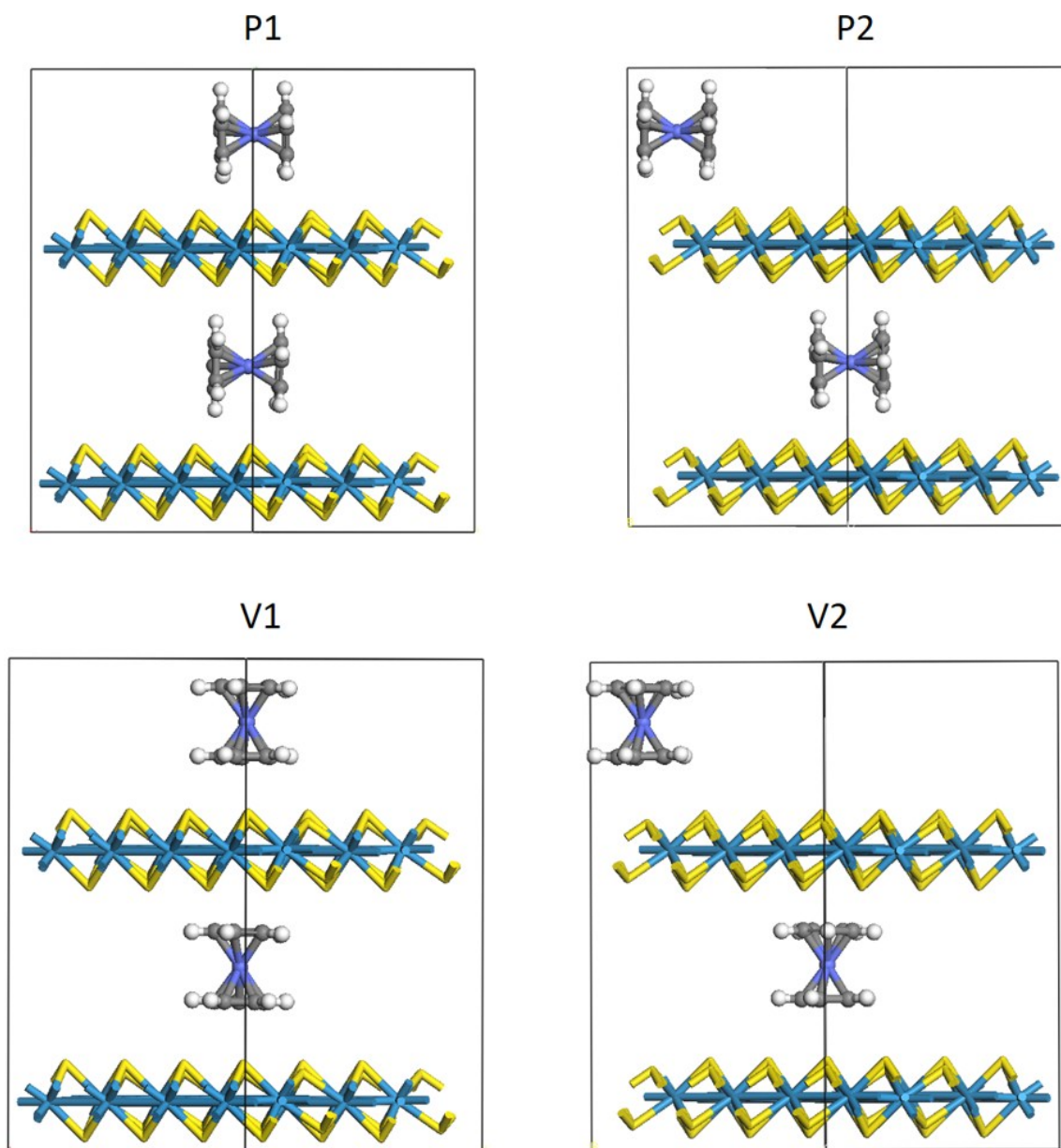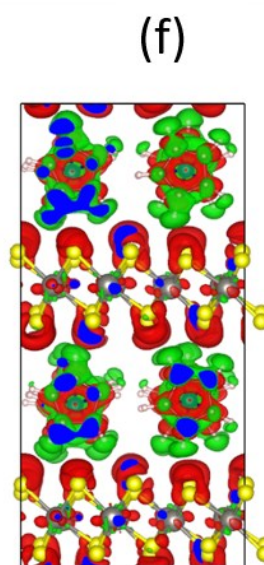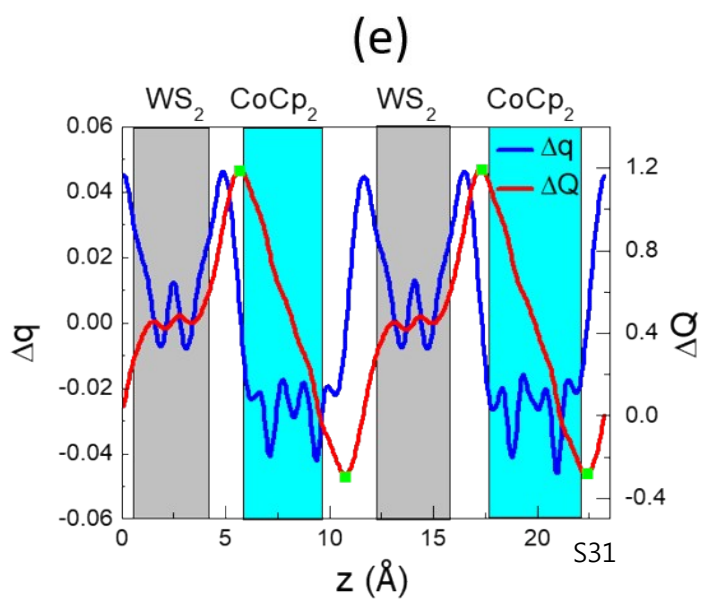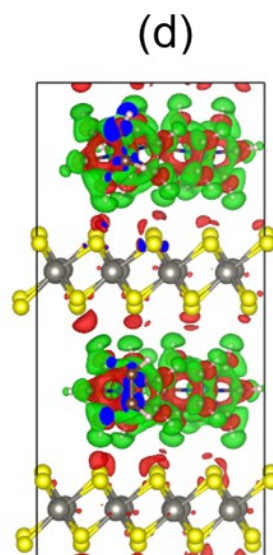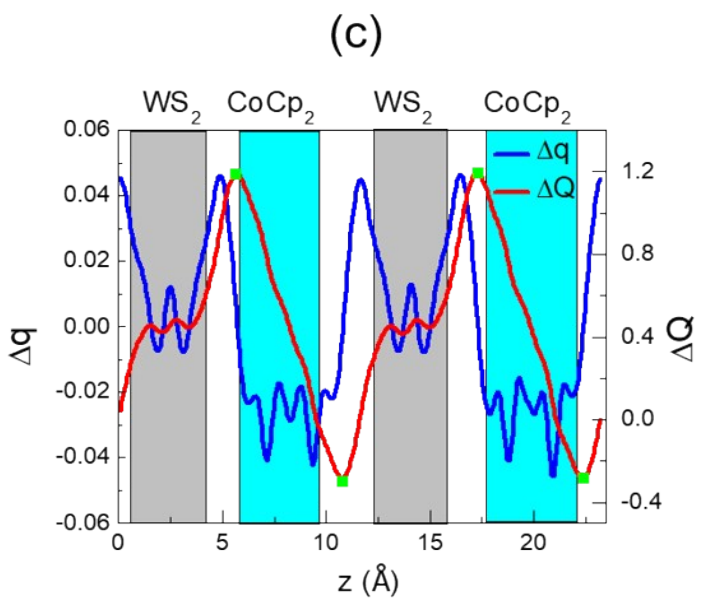
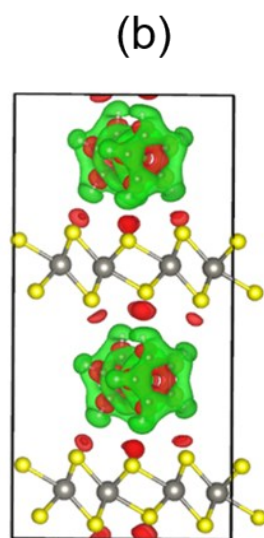**Figure S13**. Structure of P1, P2, V1, and V2 configuration (4×4) $2WS_2$-$CoCp_2$-2. Turquoise, yellow, blue, grey, and white balls represent the W, S, Co, C, and H atoms, respectively.
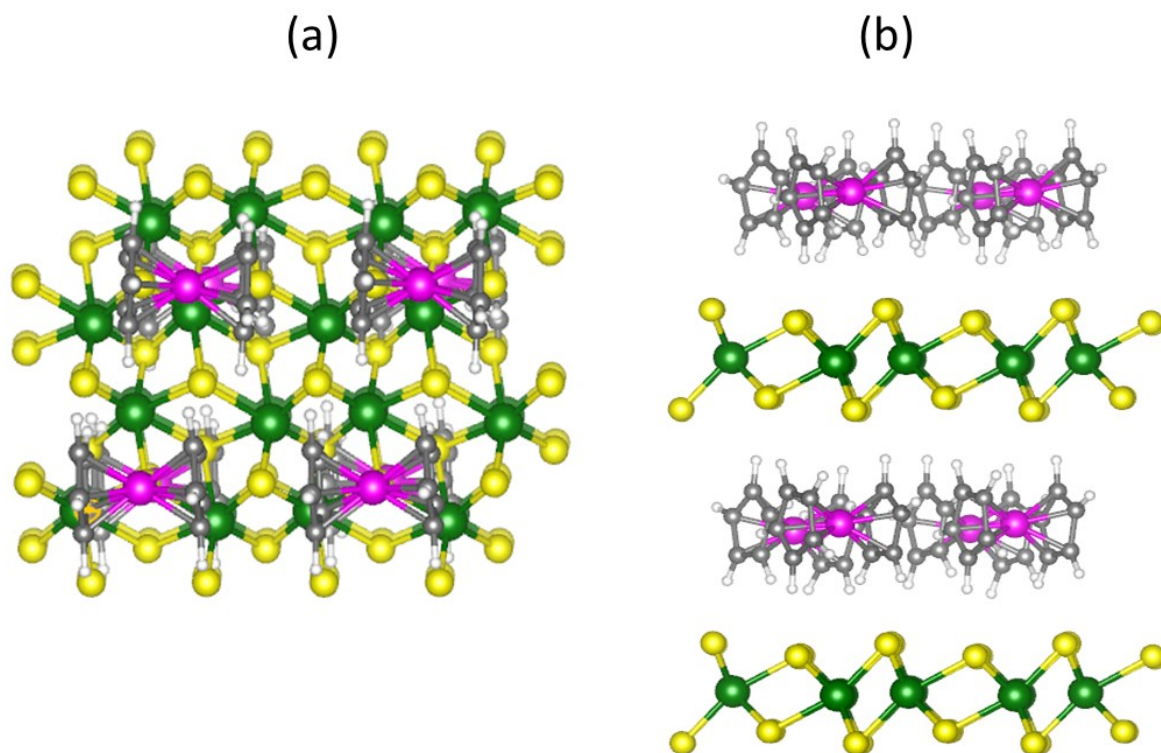
Figure S14. Structure (ball-and-stick model) of 1T′ phase (4×4)2WS$_2$-CoCp$_2$-8 (P4 configuration) in (a) top and (b) side views. Green, yellow, pink, gray, and white balls represent the W, S, Co, C, and H atoms, respectively.

(a)

(b)

(c)

(d)

(e)

(f)

S31
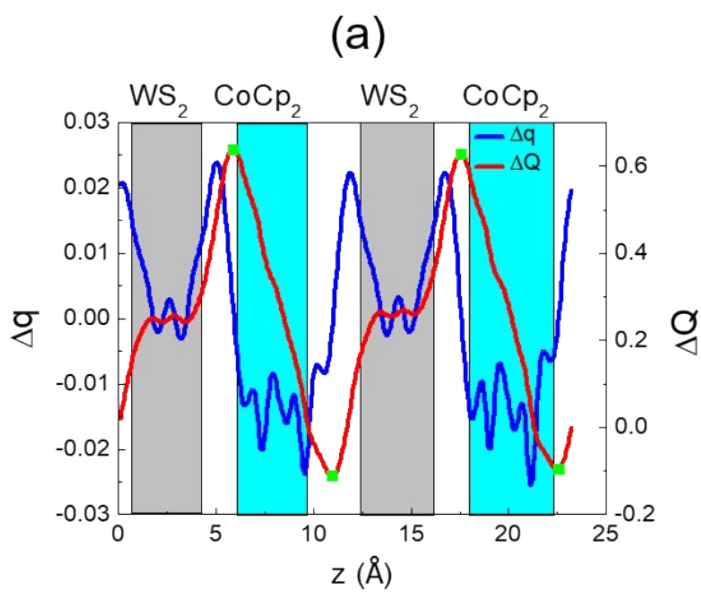
**Figure S15**. (a, c, e) Δq and ΔQ of (4×4) 2WS$_2$-CoCp$_2$-2, (4×4) 2WS$_2$-CoCp$_2$-4, and (4×4) 2WS$_2$-CoCp$_2$-8 versus z: z_{min} and z_{max} values corresponding to $Q_{min}(z)$ and $Q_{max}(z)$ are shown by filled squares (■), respectively. (b, d, f) The differential charge density $\Delta\rho(x, y, z)$ contour plot: charge accumulation and depletion regions are represented by red and green colors, respectively.

Following our previous studies, the amount of the charge transfer was calculated. The change in electron density (expressed in e Å^{-3}) along the c (= z) axis generated by the intercalation process was defined as $\Delta\rho = \rho(z)\{WS_2\text{-}CoCp_2\} - \rho(z)\{WS_2\} - \rho(z)\{CoCp_2\}$, averaged over the xy plane in a supercell.

The total electron density change (e) was defined as $\Delta q(z) = \Delta\rho(z)\Delta V$, where ΔV is the volume of a fine grid, *i.e.*, $\Delta V = V_{cell}/N_c$, in which V_{cell} is the total volume of the supercell and N_c is the number of fine grids. The thickness of each WS$_2$ layer was defined on the basis of the z coordinates of the S atoms in the upper and lower sublayers (S$_L$ and S$_U$), with $z(S_L) < z(S_U)$. The thickness of CoCp$_2$ molecules was obtained from the minimum and maximum z coordinates of its atoms. The actual thickness might be larger than that obtained using this definition, if the finite atomic size is taken into account. In addition, $Q(z)$, displayed on the right vertical axis represents the accumulated excess charge in the interval [0, z]: $Q(z) = \sum_0^{z'<z} \Delta q(z')$,

i.e., the integration of charge difference $\Delta q(z')$ within $z' < z < c$. The amount of charge transfer was defined as $\Delta Q = Q_{max} - Q_{min}$, where Q_{max} and Q_{min} correspond to the maximum and minimum charge values in the regions (marked by ■) adjacent to the WS$_2$ layers and CoCp$_2$ molecules, respectively. The ΔQ value per CoCp$_2$ is 0.75e, 0.75e, and 0.63e, respectively, for CoCp$_2$-2, CoCp$_2$-4, and CoCp$_2$-8 complexes.
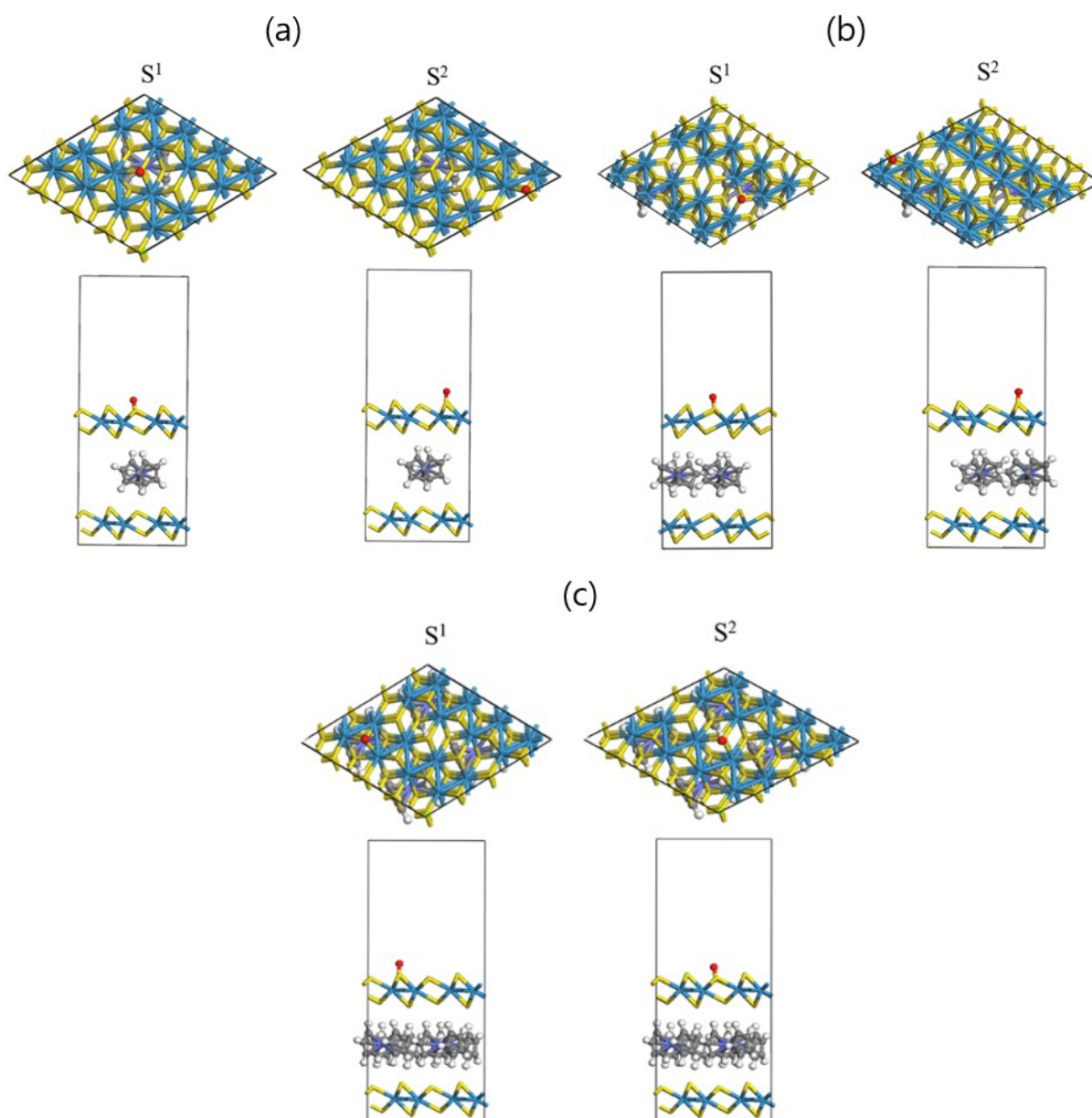
Figure S16. Structures of (a) (4×4) 2WS$_2$-CoCp$_2$-2, (b) (4×4) 2WS$_2$-CoCp$_2$-4, and (c) (4×4) 2WS$_2$-CoCp$_2$-8 in slab geometry, showing the two different adsorption sites (S^1 and S^2) for an H$^+$ ion (red balls) for Volmer reaction. Turquoise, yellow, blue, grey, and white balls represent the W, S, Co, C, and H atoms, respectively. The top and side views are shown. The red ball denotes the H atoms adsorbed on the S atoms.

IV. Reference

S1. T. P. Prasad, E. Diemann and A. Müller, *J. Inorg. Nucl. Chem.*,1973, **35**, 1895-1904.

S2. C. C. L. McCrory, S. Jung, I. M. Ferrer, S. M. Chatman, J. C. Peters and T. F. Jaramillo, *J. Am. Chem. Soc.*, 2015, **137**, 4347-4357.

S3. Y. Yin, J. Han, Y. Zhang, X. Zhang, P. Xu, Q. Yuan, L. Samad, X. Wang, Y. Wang, Z. Zhang, P. Zhang, X. Cao, B. Song and S. Jin, *J. Am. Chem. Soc.*, 2016, **138**, 7965-7972.

S4. G. Kresse and J. Hafner, *Phys. Rev. B*, 1993, **47**, 558-561.

S5. G. Kresse and J. Furthmüller, *Phys. Rev. B*, 1996, **54**, 11169-11186.

S6. G. Kresse and D. Joubert, *Phys. Rev. B*, 1999, **59**, 1758-1775.

S7. S. Grimme, *J. Comput. Chem.*, 2006, **27**, 1787-1799.

S8. G. Henkelman, B. P. Uberuaga and H. Jónsson, *J. Chem. Phys.*, 2000, **113**, 9901-9904.

S9. D. Voiry, H. Yamaguchi, J. Li, R. Silva, D. C. B. Alves, T. Fujita, M. Chen, T. Asefa, V. B. Shenoy, G. Eda and M. Chhowalla, *Nat. Mater.*, 2013, **12**, 850-855.

S10. J. Lin, Z. Peng, G. Wang, D. Zakhidov, E. Larios, M. J. Yacaman and J. M. Tour, *Adv. Energy Mater.*, 2014, **4**, 1301875.

S11. L. Cheng, W. Huang, Q. Gong, C. Liu, Z. Liu, Y. Li and H. Dai, *Angew. Chem. Int. Ed.*, 2014, **53**, 7860-7863.

S12. J. Duan, S. Chen, B. A. Chambers, G. G. Andersson and S. Z. Qia, *Adv. Mater.*, 2015, **27**, 4234–4241

S13. T. A. Shifa, F. Wang, Z. Cheng, X. Zhan, Z. Wang, K. Liu, M. Safdar, L. Sun and J. He, *Nanoscale*, 2015, **7**, 14760-14765.

S14. C. Sun, J. Zhang, J. Ma, P. Liu, D. Gao, K. Tao and D. Xue, *J. Mater. Chem. A,* 2016, **4**, 11234–11238.

S15. X. Zhou, X. Yang, H. Li, M. N. Hedhili, K.-W. Huang, L.-J. Li and W. Zhang, *J. Mater. Chem. A*, 2017, **5**, 15552–15558.

S16. K. Yang, X. Wang, H. Li, B. Chen, X. Zhang, S. Li, N. Wang, H. Zhang, X. Huang and W. Huang, *Nanoscale*, 2017, **9**, 5102-5109.

S17. Z. Liu, N. Li, C. Su, H. Zhao, L. Xu, Z. Yin, J. Li and Y. Du, *Nano Energy*, 2018, **50**, 176-181.

S18. X. Shi, M. Fields, J. Park, J. M. McEnaney, H. Yan, Y. Zhang, C. Tsai, T. F. Jaramillo, R. Sinclair, J. K. Nørskov and X. Zheng, *Energy Environ. Sci.*, 2018, **11**, 2270-2277.

S19. D. G. Clerc and D. A. Cleary, *Chem. Mater.*, 1992, **4**, 1344-1348; 1994, **6**, 13-14.

S20. T. P. Gerasimova and S. A. Katsyuba, *J. Organometal. Chem.*, 2015, **776**, 30-34.

S21 K. Nakamoto, Infrared and Raman Spectra of Inorganic and Coordination Compounds.4th Ed. Jon & Wiley Sons (1986).

S22. D. A. Cleary and A. H. Francis, *J. Phys. Chem.*, 1985, **89**, 97-100.

S23. Z. Liu, N. Li, C. Su, H. Zhao, L. Xu, Z. Yin, J. Li and Y. Du, *Nano Energy*, 2018, **50**, 176-181.